Proceedings World Geothermal Congress 2020+1
Reykjavik, Iceland, April - October 2021

# Uncertainty Quantification of Realistic Geothermal Reservoir

Yang Wang[1], Mark Khait[1], Alexandros Daniilidis[1], Denis Voskov[1,2], Sanaz Saeid[1], David Bruhn[1,3]

[1]Delft University of Technology, Netherlands; [2]Stanford University, USA; [3]Helmholtz Center Potsdam GFZ, Germany

D.V.Voskov@tudelft.nl

**Keywords:** geothermal uncertainty quantification, Monte Carlo Simulation, GPU platform, Net Present Value, energy production

## ABSTRACT

The efficient development of a geothermal field can be largely affected by the inherent geological and physical uncertainties. In addition, uncertain operational and economic parameters will impact the profitability of a project. Systematic uncertainty quantification involving these parameters helps to determine the probability of reaching the economic targets (e.g., energy production, Net Present Value (NPV), etc.). In this study, a low-enthalpy geothermal reservoir with strong heterogeneity, located in the West Netherlands Basin, is selected as the research area.

Although a detailed geological model is constructed based on various static data including seismic and log interpretation, significant uncertainties exist in the definition of the model parameters, mainly the spatial distribution of reservoir permeability and porosity. Moreover, the fluids have not been sampled in this field and can vary from brackish to highly saline brine due to the salt concentration. Also, the heat price and operational expenditures fluctuate with the market and add up to uncertainties of the physical model when an economic analysis needs to be performed. Taking all uncertain parameters into consideration, the input data set is sampled within predefined distributions or ranges using the Monte Carlo method. Ensembles of forward simulations are powered by the GPU version of the Delft Advanced Research Terra Simulator (DARTS), which has been proven to provide high computational performance with the studied model. The uncertainty of energy production and NPV with different parameters is comprehensively investigated. The observed uncertainty inside the complex subsurface system will never be unveiled without such a detailed quantification.

## 1. INTRODUCTION

The management of energy applications related to subsurface resources should consider the uncertain parameters sufficiently. The developing strategies of subsurface systems can be adjusted after consideration of uncertainties, which have been shown in various industrial applications [Ballio and Guadagnini, 2004; Kang and Jackson, 2015; Daniilidis et al., 2017; Shetty et al., 2018]. Without exceptions, the energy production from geothermal reservoirs can be easily perturbed by the uncertainties as well.

Limited by geological measurements and samples, our knowledge about a target reservoir is generally based on data interpretation and empirical correlations. For example, the relationship between permeability and porosity is often based on empirical petrophysical correlations, while the porosity values are often interpreted from core analysis and log curves. However, the spatial distribution of permeability and porosity is highly uncertain. Besides, the physical and thermal properties of fluids (e.g., salinity, density) and rock (e.g., thermal capacity and conductivity) can vary with mineral dissolution and rock compositions at geological time scales. These variations impact the amount of energy and heat transport processes inside the reservoir. In addition, the operations of a geothermal reservoir should take the economical part into account, which directly determines the project success. However, the economical parameters (e.g., heat and electricity prices) will fluctuate with the markets, which introduce uncertainties in the comprehensive appraisal of a geothermal project.

Quantifying the influence of uncertain key parameters in advance will assist reservoir management and improve the developing schemes in time. One advantage of numerical simulations is that the reservoir response to the presence of various uncertainties during development can be inspected with ensembles of forward simulations. Monte Carlo Simulation (MCS) has been widely used to quantify the uncertainties in subsurface applications [Athens and Caers, 2019; Cremon et al., 2020; Taverniers and Tartakovsky, 2020]. MCS performs simulations with random input data in the parameter space. How representative MCS simulation results are depends on the dimension of the uncertain parameter space and the nonlinearity of the underlying model. To achieve converging results, MCS usually performs a large number of forward simulations, which requires a high-performance numerical simulation framework and abundant computation resources, especially for large models with detailed geological characterization.

A popular treatment to mitigate the computational challenges for larger models is property upscaling. Restricted by the computational resources, the simulation models are often compromised with coarse resolutions by efficient upscaling-based approaches [Chen et al., 2003; Chen and Durlofsky, 2006] in isothermal simulations. However, the heat transport in geothermal systems is governed by the interplay of thermal convection and conduction. The generally ignored or coarsely-upscaled entities (e.g., shale facies) in isothermal simulation should be carefully dealt with in geothermal systems. To the best of our knowledge, it is still an open question how to effectively upscale the non-reservoir lithologies in geothermal simulations [Perkins, 2019]. Consequently, the demanding computational workload of large models (e.g., with millions of grid blocks) remains a challenge for conventional reservoir simulators.

With the development of GPU computing architecture, high-performance computation reduces the time required for the laborious simulations to an affordable time. In this study, a general-purpose numerical simulator, called Delft Advanced Research Terra Simulator (DARTS) [DARTS, 2019], is utilized to perform geothermal simulations. DARTS is constructed within the advanced Operator-Base Linearization (OBL) framework [Voskov, 2017]. The efficiency and accuracy of DARTS for geothermal simulation have been benchmarked with state-of-the-art simulators on CPU [Wang et al., 2020a]. The recent implementation of GPU and multithread CPU versions of DARTS [Khait and Voskov, 2017, Khait et al., 2020] have largely improved the simulation performance. A benchmark study [Khait et al., 2020] demonstrates that the geothermal simulation with DARTS on GPU achieves an order of magnitude faster speed than a single-thread CPU simulation.

In this study, systematic uncertainty quantification is performed for a real geothermal reservoir with detailed reservoir characterizations. MCS is selected to investigate the uncertainty of energy production and Net Present Value (NPV) with multiple parameters. The large ensembles of forward simulations are executed on the GPU version of DARTS. In the following content of the paper, the geological, mathematical and economical models of this work are first introduced, followed by a description of input parameters for investigated uncertain parameters. After a series of forward simulations, a convergence study is performed to examine the MCS convergence. Then, a detailed uncertainty analysis is presented based on the numerical results, followed by discussion and conclusions.

## 2. MODEL

### 2.1 Geological model

The geological model is provided by a service company responsible for the geothermal field development. The study area is located in the West Netherlands Basin, which is an inverted rift basin. Sediments in this basin range in age from Jurassic to recent and are overlying Triassic and older sediments. The Upper Jurassic and Lower Cretaceous start with the continental sediments of the Nieuwerkerk Formation and Vlieland sandstone Formation. These sediments were deposited in subsiding half-grabens, while adjacent highs were subjected to erosion [PanTerra Geoconsultants, 2018]. In these formations two main reservoir layers have been observed, Berkel Sandstone and Delft Sandstone. Approximately 3.2 million grid cells are used to characterize the model under geological scale.

The Berkel Sandstone Member and Berkel Sands-Claystone Member have a shallow marine depositional setting. The facies range from upper shoreface to lower shoreface of a coastal-barrier system. Lateral continuity is often good and cementation low. The permeability of the sands is good to excellent ranging from 400 to >1000 mD.

The Delft Sandstone is interpreted to be deposited as stacked distributary-channel deposits in a lower coastal plain setting resulting in massive sandstone sequences. The thickness of the Delft Sandstone is influenced by the syn-rift deposition of the sediments and therefore the Delft Sandstone is of variable thickness, a thickness up to 130m is observed. The sandstone consists of fine- to coarse-grained sand, the lateral continuity is difficult to predict. Porosities range from 10% to 27% and permeabilities from 40 to 2000 mD.

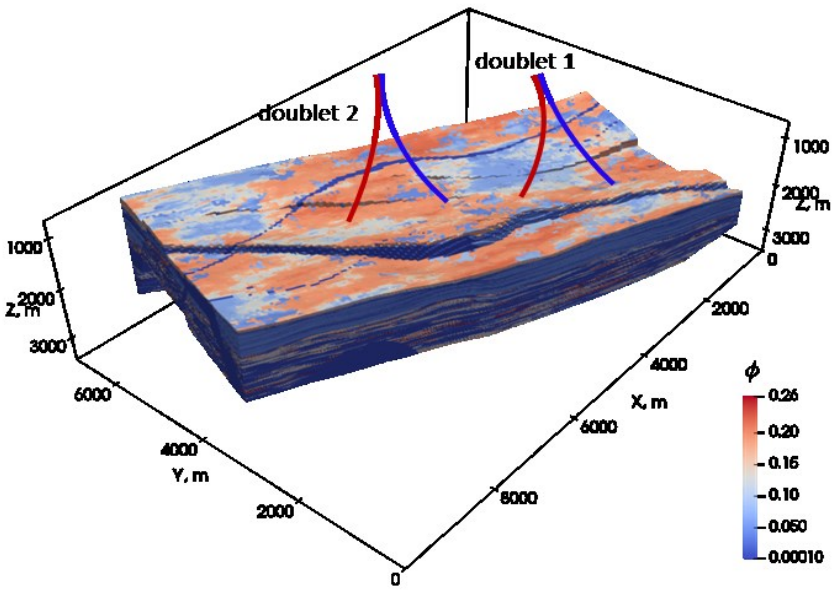


**Figure 1: Porosity distribution of the target geothermal reservoir. The model is amplified 1.5 times along the vertical direction to show the heterogeneity of the reservoir in detail. The well trajectories are connecting the following blocks in top and bottom layers respectively: I1 (51, 58) - (48, 50); P1 (76, 53) - (82, 49); I2 (94, 44) - (111, 37); P2 (124, 39) - (144, 30). The red curve represents the production well, the blue curve represents the injection well.**

The model extends along horizontal direction by 9000m × 4200m. Two doublets are placed in the reservoir and operated with a constant rate control. Since it is difficult to predict the lateral continuity, the reservoir boundary condition is defined as no-flow. Table 1 provides some basic parameter settings of the model.

**Table 1**. **Thermal and hydraulic properties of the geothermal reservoir.**

| Parameters | Unit | Values |
|---|---|---|
| Porosity (min, max) | - | ($10^{-5}$, 0.256) |
| Permeability (min, max) | mD | (0.004, 1308) |
| Shale heat capacity | kJ/m$^3$/K | 2300 |
| Sandstone heat capacity | kJ/m$^3$/K | 2450 |
| Initial temperature | K | 348.15 |
| Initial pressure | bars | 200 |
| Rate (doublet 1) | m$^3$/h | 208 |
| Rate (doublet 2) | m$^3$/h | 208 |

### 2.2 Numerical modeling

The general mass and energy conservation equations are taken to model the dynamic flow and transport processes during the development. In low-enthalpy geothermal reservoirs, brackish to highly saline brine is often encountered and used as working fluids with some chemical additives. Without loss of generality, the saline brine is chosen as the heat carrier here.

$$\frac{\partial}{\partial t}(\phi\rho_f) - div(\rho_f u_f) + \rho_f \tilde{q_f} = 0\,, \tag{1}$$

$$\frac{\partial}{\partial t}(\phi U_f + (1-\phi)U_r) - div(h_f \rho_f u_f) + div(\kappa \nabla T) + h_f \rho_f \tilde{q_f} = 0\,, \tag{2}$$

where Eq. 1 is the mass conservation equation and Eq. 2 is the energy conservation equation. $\phi$ is porosity, $\rho_f$ is fluid density [kg/m$^3$], $u_f$ is the fluid flow velocity [m/s], $\tilde{q_f}$ is the fluid source/sink term per volume [1/s], $U_f$ is fluid internal energy [kJ/m$^3$], $U_r$ is rock internal energy [kJ/m$^3$], $h_f$ is fluid enthalpy [kJ/kg], and $\kappa$ is volume-weighted thermal conductivity of rock and fluid [kJ/m/day/K].

The different quantities in Eq. 1-2 are defined as follows: the fluid internal energy per volume is expressed as:

$$U_f = \rho_f h_f\,, \tag{3}$$

and the rock internal energy per volume is expressed as:

$$U_r = C_r(T - T_{ref})\,, \tag{4}$$

where $C_r$ is the volumetric heat capacity of rock [kJ/m$^3$/K], $T_{ref}$ is the reference temperature [K]. The rock is compressible, which is reflected by the change of porosity through:

$$\phi = \phi_0(1 + c_r(p - p_{ref}))\,, \tag{5}$$

where $\phi_0$ is the initial porosity, $c_r$ is the rock compressibility [1/bar] and $p_{ref}$ is the reference pressure [bar]. In addition, Darcy's law is used to describe the fluid flow in the reservoir,

$$u_j = \frac{K}{\mu_j}(\nabla p_f - \gamma \nabla D), \tag{6}$$

where: $K$ is permeability [mD], $\mu_f$ is phase viscosity [mPa·s], $p_f$ is fluid pressure [bars], $\gamma$ is the fluid specific weight [N/m$^3$], and $D$ is depth [m].

The governing equation systems are solved in a fully coupled way in DARTS, where a general unstructured mesh combined with backward Euler timestep strategy are used to perform the spatial and temporal discretization. Besides, the advanced Operator-Based Linearization (OBL) approach [Voskov, 2017] is incorporated in DARTS [Khait and Voskov, 2018] to discretize the physical space, which highly improves the simulation efficiency with enough accuracy. More detailed implementation and applications of DARTS can be found in Khait (2019).

### 2.3 Economic model

To perform the economic analysis, we take the model from Daniilidis et al. (2020). The power [W] produced from the well is computed according to

$$P_{well} = Q\rho_f h_f\,, \tag{7}$$

in which Q is the flow rate [m$^3$/s]. The required pump power [W] only considers the pressure drop in the reservoir,

$$P_{pump} = \frac{\Delta P\, Q}{\eta}, \tag{8}$$

where $\Delta P$ is the pressure difference between the injection and production wells [Pa] and $\eta$ is the pump efficiency. The total system power is evaluated as

$$P_{system} = P_{prod} - P_{inj} - P_{pump}, \tag{9}$$

The cumulative energy produced from the system is computed using

$$E_{cum} = \sum_{t=0}^{n} P_{well_t}, \tag{10}$$

where $n$ is the project time, $t$ is the specific year. The cost of drilling the well is computed according to

$$C_{well} = 375000 + 1150Z + 0.3Z^2, \tag{11}$$

where $Z$ is the measured depth along the wellbore. The NPV is calculated as [Daniilidis et al., 2017]

$$\text{NPV} = \sum_{t=0}^{n} \frac{CF_t}{(1+r)^t}, \tag{12}$$

where $CF$ is the cash flow on a yearly basis, $r$ is the discount rate. Cash flow simply means the difference between income and cost during a certain period of time. The cumulative produced power generates income based on the heat price, while the pump power costs are computed based on the electricity price. In order to evaluate the combined system, the generated energy is first calculated on a doublet basis. The aggregated results are then used for the NPV calculations, over one year intervals.

## 3. UNCERTAIN PARAMETERS

### 3.1 Porosity-permeability realizations

In our study, 100 realizations have been generated based on variation of the seed parameter in the base case facies model [Saeid et al., 2020]. The mean and standard deviation of parameters was kept as delivered and only the spatial distribution has been varied. Initially, the facies have been generated using sequential indicator simulation for the Berkel Sandstone and object modeling for the channelized Delft Sandstone. Porosities have been generated by using Sequential Gaussian Simulation and permeabilities have been generated using co-kriging of porosity.

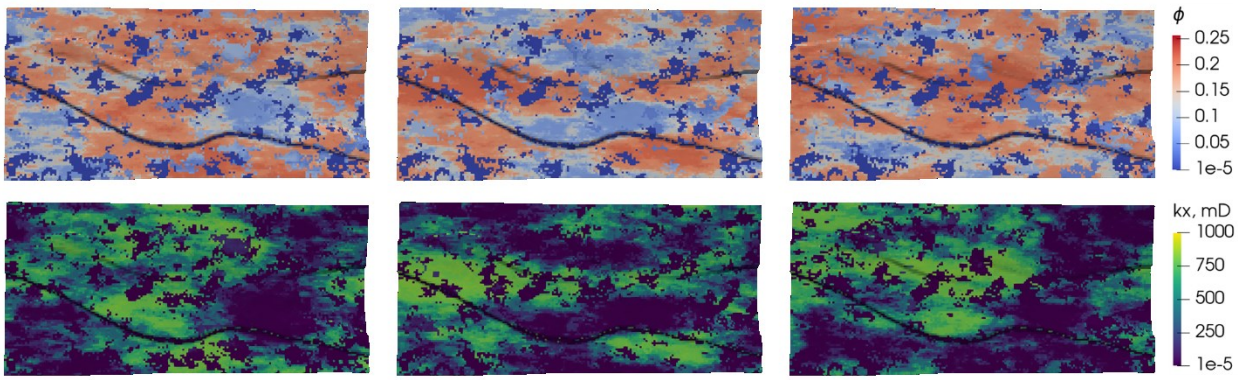


**Figure 2: Top view of the porosity and permeability distribution of three model realizations. The first row represents the porosity distribution, while the second row represents the corresponding permeability distribution.**

### 3.2 Salinity

According to Batzle and Wang (1992), the brine density as a function of salinity, temperature and pressure is described as,

$$\rho_s = \rho_w + S\left[0.668 + 0.44S + 1e^{-6}\left(300P - 2400PS + T(80 + 3T - 3300S - 13P + 47PS)\right)\right]. \tag{13}$$

The brine viscosity as a function of salinity and temperature is described as,

$$\mu_s = 0.1 + 0.333S + (1.65 + 91.9S^3)\exp[-(0.42(S^{0.8} - 0.17)^2 + 0.045)T^{0.8}], \tag{14}$$

where $\rho_s$ and $\rho_w$ are saline and water density [$\mathrm{kg/m^3}$], $\mu_s$ is viscosity [$\mathrm{mPa \cdot s}$], S is the brine mass fraction [$\mathrm{ppm/10^6}$], P is the pressure [MPa] and T is temperature [°C].

Determined by the dissolved minerals and solids, the reservoir fluid can be categorized from almost fresh water to highly saline brine [Borgia et al., 2012; Kang and Jackson, 2016]. Salinity in a geothermal system has an impact on heat propagation and the production process. Based on Saeid et al. (2015), the increase of salinity will result in a decrease in energy production and system lifetime for the investigated homogeneous reservoir. Since fluid samples are lacking, the specific salinity value is uncertain for the target reservoir. To account for the uncertainty of specific salinity, we selected a wide distribution of salinity values for our analysis, conforming to the approximate normal distribution (mean $\mu = 0.075$ ppm/1e6, standard deviation $\sigma = 0.040$ ppm/1e6).

### 3.3 Rock thermal conductivity

The rock thermal conductivity determines the speed of heat exchange when a temperature gradient is present. The importance of the thermal conductivity of different rocks for heat production and propagation in geothermal systems has been studied and stressed [Wang et al., 2020b]. It can be measured in the laboratory or at in-situ conditions. It varies with several factors, for example, mineral composition of the rock, the presence of fluids, pressure, and temperature. Prediction of the heat production should consider the introduced uncertainties in rock conductivity by these factors. The target reservoir in this study consists of two types of rocks, shale and sandstone, both of which are sedimentary rocks. The thermal conductivities of shale and sandstone (Figure 3) are assumed to follow a normal distribution. Typical numbers are selected in the normal distribution [Labus and Labus, 2018; Midttømme and Roaldset, 1999] for shale (mean $\mu = 190.1$ kJ/m/day/K, standard deviation $\sigma = 8.64$ kJ/m/day/K) and sandstone (mean $\mu = 259.2$ kJ/m/day/K, standard deviation $\sigma = 86.4$ kJ/m/day/K).

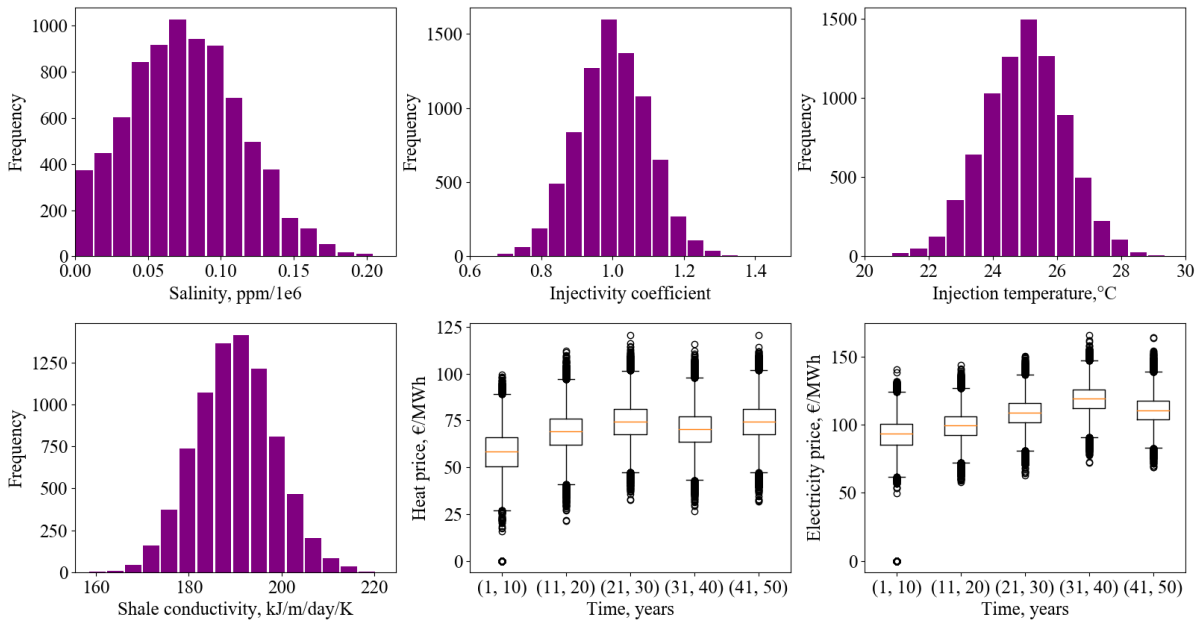


**Figure 3: Distribution of the uncertain input parameters.**

### 3.4 Injection temperature

Energy production is subject to the injection temperature, which will influence the production temperature and lifetime of the geothermal reservoir [Aliyu and Chen, 2017; Saeid et al., 2015]. The magnitude of the injection temperature can vary with heat exchange and heat losses during energy utilization and transportation. Therefore, the injection temperature is expected to fluctuate a bit. A normal distribution (mean $\mu = 25$°C, standard deviation $\sigma = 1.5$°C) is assumed to describe the uncertainty existing in the injection temperature.

### 3.5 Well injectivity

The re-injection of cold water into the reservoir can initiate mineral precipitation or thermal cracking [Benson et al., 1987] in the near-wellbore region. The injectivity of a geothermal doublet will be reduced or enhanced correspondingly. In numerical simulation, the well index (e.g., the Peaceman equation [Peaceman, 1983] $WI = \frac{2\pi\sqrt{k_x k_y}h}{\ln(r_w/r_o)}$) is used to characterize the well injectivity. Here, based on the default evaluation of well index, an injectivity coefficient is randomly sampled from a normal distribution (mean $\mu = 1$, standard deviation $\sigma = 0.1$ in Figure 3). During the simulation, the coefficient will be multiplied to the default well index to represent the uncertainty of well injectivity. In this study, since both doublets operate with constant rate, the well injectivity will influence the pressure difference within each doublet. Therefore, the required pumping energy will be different.

### 3.6 Economics

Varying with the energy source and providers, the heat and electricity prices will fluctuate within the studied period. To more accurately examine the uncertain impact of heat and electricity prices on NPV, the 50-years simulation time has been divided into sub-intervals. Within each sub-interval, it is assumed the prices will fluctuate around a mean value within a normal distribution. The prices of each year within this interval will be sampled from the normal distribution. The distribution of heat and electricity prices is shown in Figure 3. The relevant parameters for NPV calculation are listed in Table 2.

**Table 2: Parameters in NPV calculation.**

| Parameters | Unit | Values |
|---|---|---|
| Pump cost | k€ | 500 |
| Pump lifetime | years | 5 |
| Pump efficiency | % | 60 |
| OpEx (% of CapEx) | % | 5 |
| Discount rate | % | 10 |

## 4. CONVERGENCE ANALYSIS

Though it is difficult to set general criteria to calibrate the convergence of MCS, the results are expected to reach statistical convergence when the amount of samples is large enough [Ballio and Guadagnini, 2004]. The convergence rate may vary with the studied problem and variables. In this study, the energy production and NPV are two of the most concerned parameters. We consider the MCS as converged once these two parameters reach certain converged values.

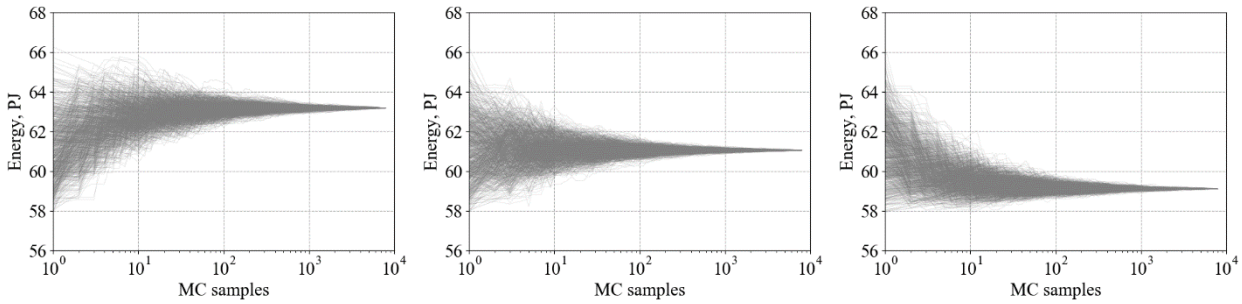


**Figure 4: P10, P50 and P90 of the cumulative energy production of 50 years.**

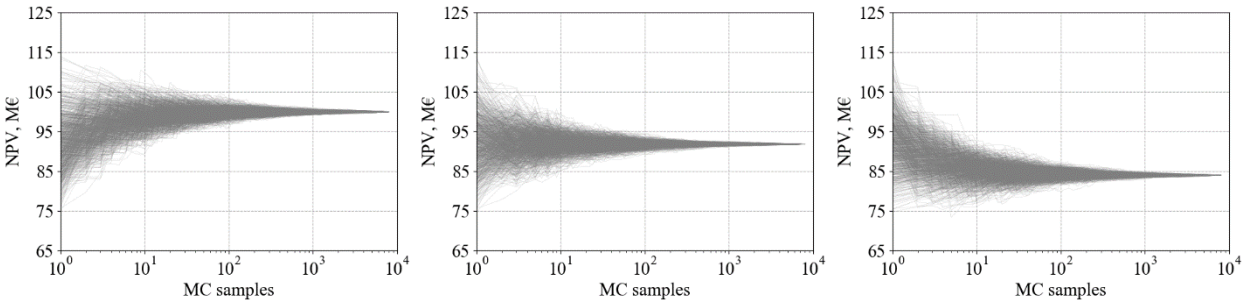


**Figure 5: P10, P50 and P90 of the NPV of 50 years.**

Figure 4 and Figure 5 plot the P10, P50 and P90 of the energy production and NPV with increasing number of MC samples. Figure 4a shows an example of MCS convergence of P10. Based on the daily energy production rate, total energy production of each MC sample can be evaluated at the end of the simulation. The energy production of all realizations is then collected as a data set. With the increasing counting of MC samples, the 10% probability of the counted data are sequentially calculated, which in the end generates one curve in Figure 4a. The data set is then randomly shuffled, and the 10% probability is re-evaluated correspondingly for multiple times. Figure 4a is made up of all these evaluations, with similar procedures for other plots in Figure 4 and Figure 5. A wide spreading of produced energy and NPV is noticed while the number of realizations is limited. To get representative values of energy and NPV, a minimum of 2000 realizations are required in our study to converge MCS for a given quantile. The P10, P50 and P90 values of total produced energy in our study are 63.2, 61 and 59.1 PJ respectively, while the P10, P50 and P90 values of total NPV are 100, 92 and 84 M€ respectively.

In addition, it is essential to check the convergence of the values for the concerned parameters, as the other indication for MCS convergence. A convergence is assumed to be reached if the distribution stays stable with increasing the number of MC realizations. Figure 6 shows $L_2$ norm of the difference between energy and NPV distributions in the MCS process. The $L_2$ norm is calculated by $||X_n - X_{n-1}||_2$, where $X_n$ and $X_{n-1}$ are the normalized distribution at current and previous computation steps. As expected, the distribution difference drops with the increase of MC samplings. With an approximate 2000 realizations, the distribution difference becomes smaller than 1%, which is regarded as converged.

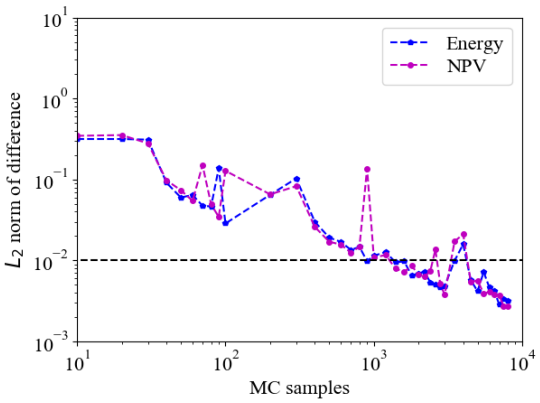


**Figure 6: $L_2$ norm of the distribution difference with the increase of MC samples for produced energy and NPV.**

## 5. NUMERICAL RESULTS

### 5.1 Production temperature and pressure drop

Figure 7 displays the production temperature of all realizations for both doublets. A maximum temperature difference of 8 K at 50 years of operation for doublet 1 is observed. The production temperature of doublet 1 is largely impacted by the uncertain parameters. A temperature of 340.5 K (P50) has the highest probability at the end of simulation. As a comparison, the spread in production temperature after 50 years for doublet 2 is only 4 degrees, demonstrating a relatively weak temperature response to the uncertainty of input parameters. In addition, the overall temperature drop for doublet 2 is less than for doublet 1, which is an indication of well interference. The well interference suggests that there is a diversion effect of doublet 1 to the injection well of doublet 2, which influences the thermal propagation of doublet 2. As is shown in Figure 1, the injection well of doublet 2 is close to the producer of doublet 1, which indicates the water supply of doublet 2 to doublet 1. Therefore, the cold front propagation becomes slower in doublet 2.

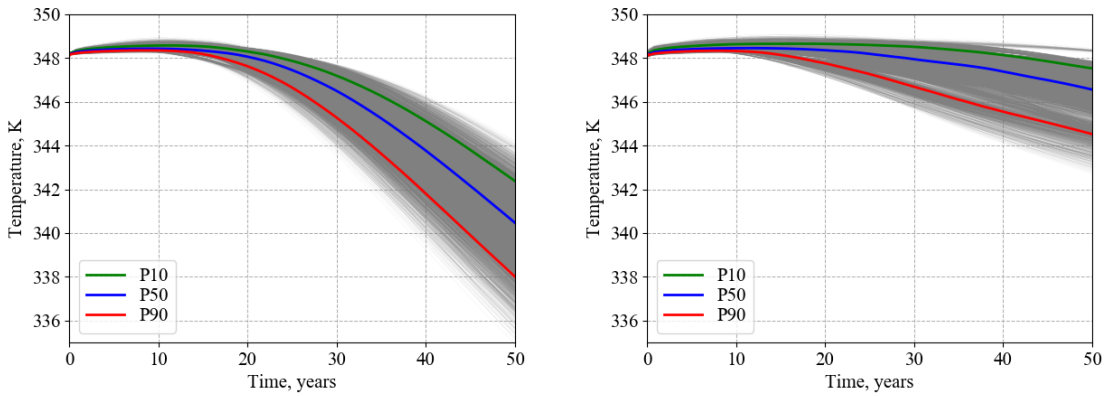


(a) doublet 1 (b) doublet 2

**Figure 7: Production temperature of doublet 1 and 2, and the corresponding P10, P50, P90 production temperature curves.**

Figure 8 shows the drop of Bottom Hole Pressure (BHP) of all realizations for both doublets. The pressure drop of doublet 1 after 50 years ranges from 35 bars to 80 bars (Figure 8a), where a 54-bars drop represents the P50 value. The pressure drop of doublet 2 varies from 45 bars to 145 bars, where 80-bars is the most probable pressure drop (P50). This shows that the uncertain parameters have a much stronger impact on the pressure calculation for doublet 2. In addition, the magnitude of pressure drop calculated for doublet 2 is, on average, larger than for doublet 1. This indicates that the average permeability is smaller within the controlled area of doublet 2, as the distance between the two wells in both doublets is similar.

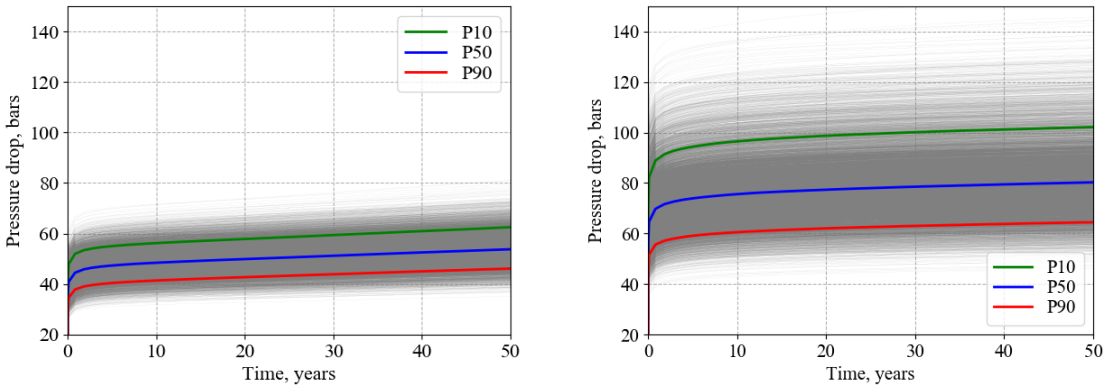


(a) doublet 1 (b) doublet 2

**Figure 8: Pressure drop of doublet 1 and 2, and the corresponding P10, P50, P90 of pressure drop. Here, the pressure drop refers to the pressure difference between injector and producer within one doublet.**

### 5.2 Energy, NPV and break-even time

Figure 9 displays the distribution of the cumulative produced energy and NPV of all realizations at the end of the simulations. While the NPV follows a classic Gaussian-type distribution, the energy follows a beta-like distribution. Since the input parameters are sampled with normal distributions (except the randomly sampled poro-perm realizations), the observed system response to the combined input seems predictable, although the individual impact of each input parameter can be different, as discussed below. However, for complex subsurface systems as in this study, the output from ensemble models will be highly case-dependent, which is difficult to predict without systematic forward simulations. Assumptions made in this study, such as fixed production rate of each doublet, reduce the variability of the final results and limit the uncertainty analysis.

After 50 years, the difference of energy production between P10 and P90 is 4.1 PJ, while the spread of NPV between P10 and P90 is 16 M€. To quantify the uncertainties, we define an uncertain factor (α) as the ratio of (P10, P90) difference and P50 value, $\alpha = \frac{(X_{P10} - X_{P90})}{X_{P50}} \times 100\%$. With this definition, the uncertainty of NPV (17.39%) is much larger than that of produced energy (6.72%). On the one hand, it is because two additional uncertain input parameters (heat and electricity price) are considered in the NPV evaluation. On the other hand, the NPV calculation takes more factors into account (e.g., pressure drop within a doublet, injected energy, etc.), which will be discussed in the following section. As a comparison, the produced energy is more correlated with the heat transport and thermal exchange inside the reservoir.

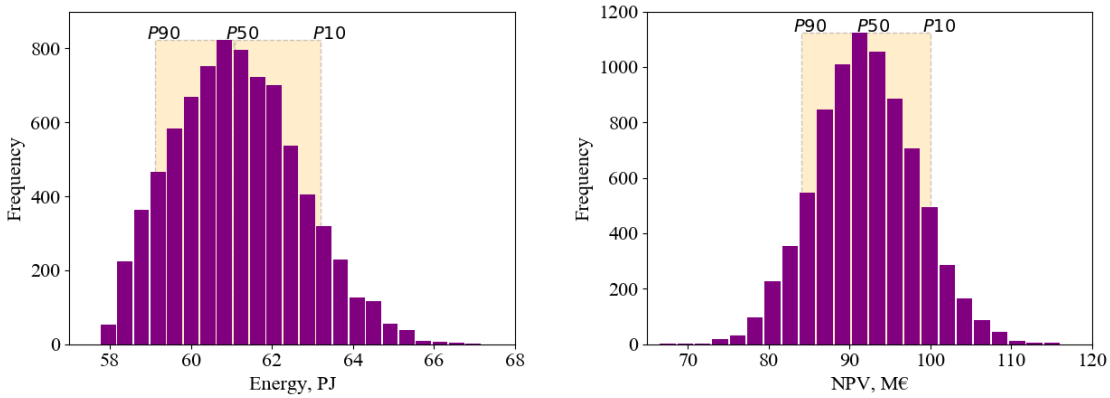


**Figure 9: Energy and NPV distributions of the system after 50 years. The samples falling between P10 and P90 of each distribution are marked in orange.**

Figure 10 displays the cumulative NPV of all realizations and the converged break-even time. As is shown in Figure 10a, a large cash investment is required at the beginning of the project, including drilling and equipment costs. Based on a 10% discount rate, the NPV already experiences decelerated growth at the end of the 30th year and reaches a plateau within the last 20 years of production.

Break-even time refers to the amount of time required for the discounted cash flows generated by a project to match its initial cost. With the selected production strategy, a break-even time of less than 2 years is expected, which will be an attractive information for the investors. This project will become net profitable after 2 years and no risk factors are foreseeable with the uncertainty of the parameters considered in this study.

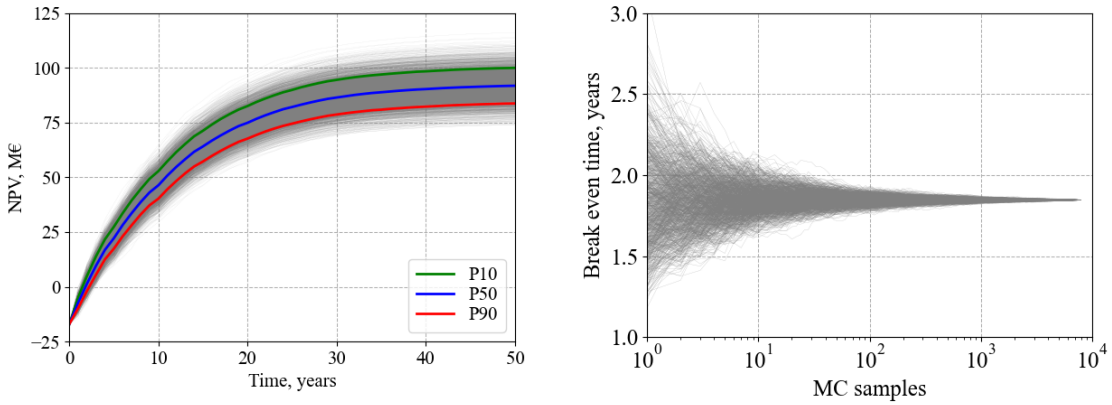


**Figure 10: Cumulative NPV and break-even time of all realizations along the simulation.**

### 5.3 Uncertainty of system output to individual parameters

The output uncertainty to aggregated input parameters has been discussed in the previous parts. This section will show the influence of individual uncertain parameters to energy and NPV under the presence of other uncertain parameters.

In Figure 11, the independent impact of six parameters (poro-perm realization, salinity, injectivity coefficient, injection temperature, shale and sandstone conductivity) to total energy production is listed. In each subplot, values of the investigated parameter are first divided into sub-intervals, which are used as filters for the MC samples. The energy distribution of the filtered MC samples is then plotted against each sub-interval correspondingly. The sensitivity of energy to different parameters can be observed within these plots.

Influenced by other input parameters and by the number of filtered realizations, the distribution of produced energy varies significantly within each subplot. However, the mean values of energy are not sensitive to individual parameters, except to the salinity. The energy production is directly associated with the fluid density Eq. (7), which is the function of salinity Eq. (13). Therefore, the shift of mean energy value to salinity is straightforward. The injectivity coefficient mainly influences the operating pressure difference within each doublet and the energy production is not visibly affected under the constant rate operation. In fluvial systems, shale influences energy production via thermal conduction as an additional heat source. In our previous work with the same model [Wang et al., 2020b], we analyzed the significant influence of shale on the energy production by including and excluding the shale facies. However, the sensitivity of energy production to the magnitude of shale conductivity was not studied before. In Figure 11, the overall variation of produced energy with thermal conductivity is not obvious for typical conductivity ranges.

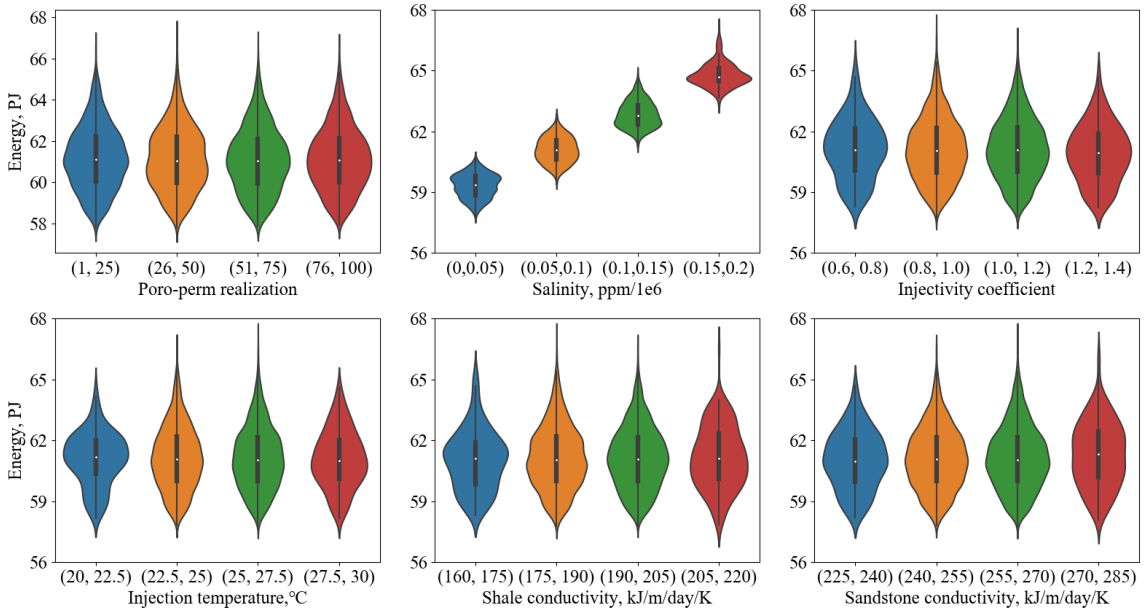


**Figure 11: The uncertainty of energy production to single uncertain input parameters.**

Similarly, Figure 12 displays the uncertainty of NPV to six parameters (poro-perm realization, salinity, injectivity coefficient, injection temperature, mean heat and electricity price). Note that since the heat and electricity prices fluctuate with time, their mean value during the total 50-years period is collected for each MC realization, composing the data set of mean prices. We can see a large uncertainty of mean NPV with the variation of salinity, injection temperature and mean heat price. This also explains the observation of larger uncertainty in NPV than in energy from the previous section. Since NPV is positively correlated with generated energy, it

increases with salinity and similarly with heat price as well. The injection temperature influences NPV via the system power (Eq. (9)) as higher injection temperature causes lower system power and therefore, lower NPV. The electricity cost only takes a small portion in the total NPV calculation, which is verified by the short break-even time (in Figure 10) of this project.

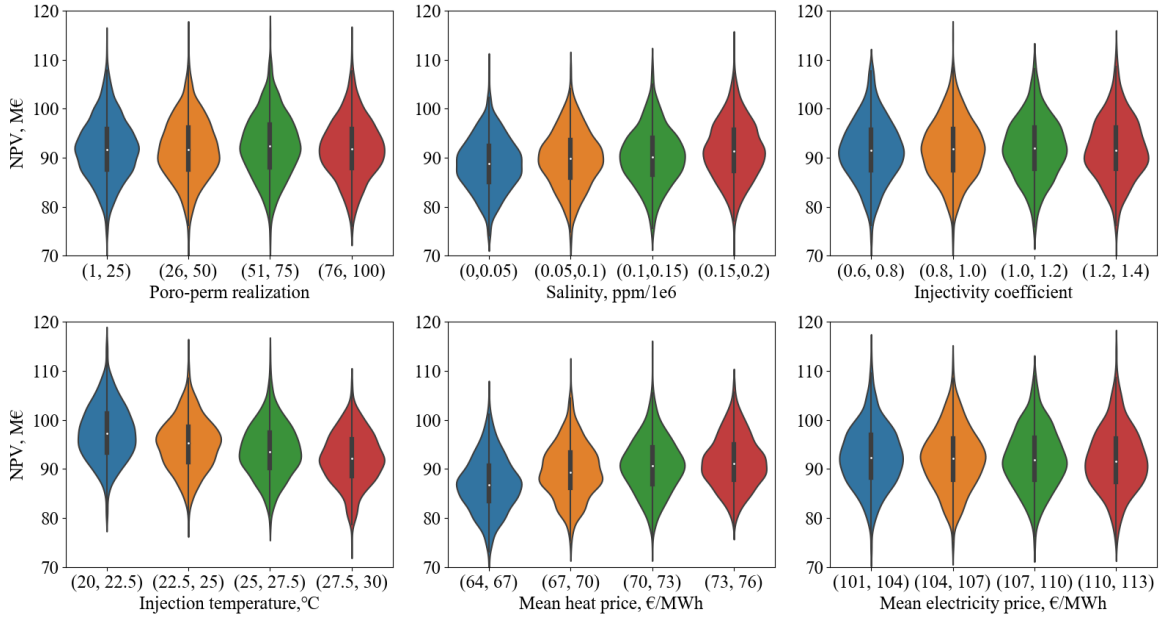


**Figure 12: The uncertainty of NPV to single uncertain input parameter.**

### 5.4 Simulation time

Owing to the high computing performance of the GPU version of DARTS, the mean simulation time for a 50-years simulation (with a maximum timestep of one year) stabilizes at 3.49 minutes on the Titan RTX GPU card. According to Khait et al. (2020), the benchmarked simulation with the same model on single thread CPU of Intel Core i7-8086K requires about 80 mins to run for 100 years (or approximately 40 mins for a 50-years simulation). The performance has been improved by more than an order of magnitude. Using the Monte Carlo method, it is convenient to run multiple simulations in parallel. This uncertainty quantification study was performed on 16 GPU cards simultaneously. The total 8000 simulations were finished within 30 hours.

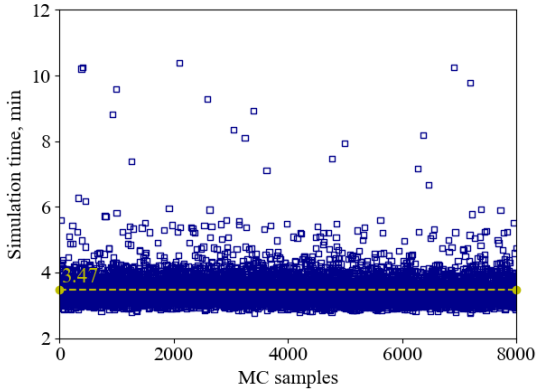


**Figure 13: Simulation time of all realizations. The yellow dash line marks the mean value of simulation time at 3.47 mins.**

## 6. CONCLUSION

In this paper, a systematic uncertainty quantification for a real geothermal reservoir from the West Netherlands Basin has been studied. The geological model entails detailed reservoir characterization with high-resolution meshes, which provides a unique model representation for the real application. The uncertain physical, geological and economical parameters are incorporated into the investigation, where the Monte Carlo method is used for parameter sampling. The high performance of the GPU version of DARTS and the parallelization of the Monte Carlo method guarantee the large ensembles of forward simulations finished in affordable time.

The two most concerned parameters (energy and NPV) are used as indicators for the convergence of the Monte Carlo Simulation. After examination of the MCS convergence, the uncertainties of energy and NPV are discussed according to the numerical results. We found larger overall uncertainty for the NPV than for the energy, which is due to more factors included within the NPV evaluation. In real geothermal developments, the uncertain input parameters should be thoroughly considered to obtain valuable estimations of

the concerned production characteristics. The uncertainty in the mean values of energy and NPV is less sensitive to some parameters, such as shale and sandstone conductivity, which indicates it is representative enough to just use typical values for these parameters.

Through this study, we emphasize the importance of uncertainty quantification to geothermal field development by demonstrating how various uncertain parameters affect the predictions of produced energy and NPV. The aggregated impact of all these parameters cannot be recognized without systematic uncertainty quantification and ensembles of forward simulation.

**ACKNOWLEDGEMENTS**

We acknowledge SURFSara for providing us the access to their GPU cluster, Total for sponsoring DARTS-GPU research and the financial support from China Scholarship Council to Yang Wang.

**REFERENCE**

Aliyu, M., Chen, H.P., 2017. Sensitivity analysis of deep geothermal reservoir: Effect of reservoir parameters on production temperature. *Energy* 129, 101–113.

Athens, N.D., Caers, J.K., 2019. A Monte Carlo-based framework for assessing the value of information and development risk in geothermal exploration. *Applied Energy*, 256.

Ballio, F., Guadagnini, A., 2004. Convergence assessment of numerical Monte Carlo simulations in groundwater hydrology. *Water Resources Research* 40, W046031–W046035.

Batzle, M., Wang, Z., 1992. Seismic properties of pore fluids. *Geophysics* 57, 1396–1408.

Benson, S., Daggett, J., Iglesias, E., Arellano, V., Ortiz-Ramirez, J., 1987. Analysis of thermally induced permeability enhancement in geothermal injection wells, *Workshop on Geothermal Reservoir Engineering*.

Borgia, A., Pruess, K., Kneafsey, T., Oldenburg, C., Pan, L., 2012. Numerical simulation of salt precipitation in the fractures of a $CO_2$-enhanced geothermal system. *Geothermics* 44, 13–22.

Chen, Y., Durlofsky, L., 2006. Adaptive local-global upscaling for general flow scenarios in heterogeneous formations. *Transport in Porous Media* 62, 157–185.

Chen, Y., Durlofsky, L., Gerritsen, M., Wen, X., 2003b. A coupled local-global upscaling approach for simulating flow in highly heterogeneous formations. *Advanced in Water Resources* 26, 1041–1060.

Cremon, M., Christie, M., Gerritsen, M., 2020. Monte Carlo simulation for uncertainty quantification in reservoir simulation: A convergence study. *Journal of Petroleum Science and Engineering* 190.

Daniilidis, A., Alpsoy, B., Herber, R., 2017. Impact of technical and economic uncertainties on the economic performance of a deep geothermal heat system. *Renewable Energy* 114, 805–816.

Daniilidis, A., Khait, M., Saeid, S., Bruhn, D., Voskov, D., 2020. A high performance framework for the optimization of geothermal systems, comparing energy production and economic output, *World Geothermal Congress*.

DARTS, 2019. Delft Advanced Research Terra Simulator. https://darts.citg.tudelft.nl.

Gong, B., Karimi-Fard, M., Durlofsky, L., 2008. Upscaling discrete fracture characterizations to dual-porosity, dual-permeability models for efficient simulations of flow with strong gravitational effects. *SPE Journal* 13, 58–67.

James, A., Oldenburg, C., 1997. Linear and Monte Carlo uncertainty analysis for subsurface contaminant transport simulation. *Water Resources Research* 33, 2495–2508.

Kang, M., Jackson, R., 2016. Salinity of deep groundwater in California: Water quantity, quality, and protection. *Proceedings of the National Academy of Sciences of the United States of America* 113, 7768–7773.

Khait, M., Voskov, D., 2017. GPU-offloaded general purpose simulator for multiphase flow in porous media, *SPE Reservoir Simulation Conference*.

Khait, M., Voskov, D., 2018. Operator-based linearization for efficient modeling of geothermal processes. *Geothermics* 74, 7–18.

Khait, M., Voskov, D., Zaydullin, R., 2020. High performance framework for modelling of complex subsurface flow and transport applications, *17th European Conference on the Mathematics of Oil Recovery*.

Labus, M., Labus, K., 2018. Thermal conductivity and diffusivity of fine-grained sedimentary rocks. *Journal of Thermal Analysis and Calorimetry* 132, 1669–1676.

Midttømme, K., Roaldset, E., 1999. Thermal conductivity of sedimentary rocks: uncertainties in measurement and modelling. *Geological Society Special Publication* 158, 45–60.

PanTerra Geoconsultants, 2018. Project report: G1330c. Technical Report.

Peaceman, D.W., 1983. Interpretation of well-block pressures in numerical reservoir simulation with nonsquare grid blocks and anisotropic permeability. *SPE Journal* 23, 531–543.

Perkins, D., 2019. Reservoir simulation for play-based development of low enthalpy geothermal resources. Master's thesis. https://repository.tudelft.nl.

Saeid, S., Al-Khoury, R., Nick, H., Hicks, M., 2015. A prototype design model for deep low-enthalpy hydrothermal systems. *Renewable Energy* 77, 408–422.

Saeid, S., Wang, Y., A., D., Khait, M., Voskov, D., Bruhn, D., 2020. Lifetime and energy prediction of geothermal systems: Uncertainty analysis in highly heterogeneous geothermal reservoirs (Netherlands), *World Geothermal Congress*.

Scheidt, C., Caers, J., 2009. Uncertainty quantification in reservoir performance using distances and kernel methods-application to a West Africa deep water turbidite reservoir. *SPE Journal* 14, 680–692.

Shetty, S., Voskov, D., Bruhn, D.F., 2018. Numerical strategy for uncertainty quantification in low enthalpy geothermal projects, *Workshop on Geothermal Reservoir Engineering*.

Taverniers, S., Tartakovsky, D.M., 2020. Estimation of distributions via multilevel Monte Carlo with stratified sampling, *Journal of Computational Physics*, 419.

Veldkamp, J.G., Pluymaekers, M.P.D., van Wees, J.D.A.M., 2015. DoubletCalc 2D 1.0 User Manual. Technical Report.

Voskov, D., 2017. Operator-based linearization approach for modeling of multiphase multi-component flow in porous media. *Journal of Computational Physics* 337, 275–288.

Wang, Y., Voskov, D., Khait, M., Bruhn, D., 2020a. An efficient numerical simulator for geothermal simulation: A benchmark study. *Applied Energy* 264.

Wang, Y., Voskov, D., Khait, M., Saeid, S., Bruhn, D., 2020b. Influential factors to the development of low-enthalpy geothermal energy: a sensitivity study of realistic field. submitted to journal.